

# Inkjet Printed Large-Area Flexible Few-Layer Graphene Thermoelectrics

Taneli Juntunen, Henri Jussila, Mikko Ruoho, Shouhu Liu, Guohua Hu, Tom Albrow-Owen, Leonard W. T. Ng, Richard C. T. Howe, Tawfique Hasan,\* Zhipei Sun,\* and Ilkka Tittonen\*

Graphene-based organic nanocomposites have ascended as promising candidates for thermoelectric energy conversion. In order to adopt existing scalable printing methods for developing thermostable graphene-based thermoelectric devices, optimization of both the material ink and the thermoelectric properties of the resulting films are required. Here, inkjet-printed large-area flexible graphene thin films with outstanding thermoelectric properties are reported. The thermal and electronic transport properties of the films reveal the so-called phonon-glass electron-crystal character (i.e., electrical transport behavior akin to that of few-layer graphene flakes with quenched thermal transport arising from the disordered nanoporous structure). As a result, the all-graphene films show a room-temperature thermoelectric power factor of  $18.7 \mu\text{W m}^{-1} \text{K}^{-2}$ , representing over a threefold improvement to previous solution-processed all-graphene structures. The demonstration of inkjet-printed thermoelectric devices underscores the potential for future flexible, scalable, and low-cost thermoelectric applications, such as harvesting energy from body heat in wearable applications.

perspective of thermoelectricity, known to benefit from energy quantization arising from spatial confinement, as well as restricted thermal phonon propagation within the structure.<sup>[2]</sup> While the field has witnessed a steady progress in developing more efficient materials for thermoelectric energy conversion, the current high-efficiency thermoelectrics remains largely based on toxic, naturally scarce, mechanically rigid, and/or expensive solid state materials,<sup>[3,4]</sup> such as PbTe,<sup>[5]</sup> Bi<sub>2</sub>Te<sub>3</sub>,<sup>[6]</sup> and Sb<sub>2</sub>Te<sub>3</sub>.<sup>[7]</sup> These shortcomings have raised interest toward abundant and low-cost organic solutions.

As the most widely studied instance of the family of 2D materials, graphene has gained particular attention for electronic, mechanical, and photonic applications due to its unique properties,<sup>[8]</sup> including extremely large charge carrier mobility,<sup>[9]</sup> exceptionally high mechanical strength,<sup>[10]</sup>

## 1. Introduction

Nanostructured thermoelectrics has emerged as a central research field for sustainable low-grade waste heat recovery.<sup>[1]</sup> Low-dimensional systems are of particular interest from the

and ultrafast broadband optical response.<sup>[11]</sup> However, the potential of graphene as a thermoelectric material has been met with limited expectations. Indeed, the vanishing bandgap due to the semimetallic nature of graphene implies limited Seebeck coefficient,<sup>[12]</sup>  $S$ , which together with the exceptionally large in-plane thermal conductivity,<sup>[13]</sup>  $\kappa$ , of single sheet graphene leads to a modest thermoelectric conversion efficiency, as determined from the unitless figure of merit  $zT = S^2T(\rho\kappa)^{-1}$ , where  $\rho$  and  $T$  denote electrical resistivity and temperature, respectively. A number of theoretical studies have found ways to circumvent these problems by utilizing various nanostructure designs, for example, graphene nanoribbons,<sup>[14]</sup> heterostructures,<sup>[15]</sup> and nanopore structures<sup>[16]</sup> for improved Seebeck coefficient, and boundary roughness,<sup>[17]</sup> defects,<sup>[18]</sup> and isotope engineering<sup>[19]</sup> for thermal design. Some of these studies have predicted unusually large values of  $zT$  for graphene, in the range of  $zT = 2\text{--}5$  at room temperature.<sup>[12]</sup> However, most of the proposed strategies remain challenging to translate into practical devices due to the lack of required large-area fabrication techniques, and the fact that the singular intrinsic properties of graphene are notoriously undermined by the strongly quenched interflake transport in graphene nanocomposites.<sup>[20]</sup> As a result, while graphene has shown exceptional promise as a constituent in conductive polymer-based low-temperature thermoelectrics,<sup>[20,21]</sup> few studies have focused on thermostable all-graphene structures produced via scalable, solution-based methods.<sup>[4,22]</sup> Such an approach enables exploitation of the existing commercial printing processes, such as inkjet printing

T. Juntunen, Dr. H. Jussila, Dr. M. Ruoho, Prof. Z. Sun, Prof. I. Tittonen  
Department of Electronics and Nanoengineering  
Aalto University

FI-00076 Aalto, Finland

E-mail: zhipei.sun@aalto.fi; ilkka.tittonen@aalto.fi

Dr. H. Jussila, S. Liu, Dr. G. Hu, T. Albrow-Owen, L. W. T. Ng,

Dr. R. C. T. Howe, Dr. T. Hasan

Cambridge Graphene Centre

University of Cambridge

9 JJ Thomson Avenue, Cambridge CB3 0FA, UK

E-mail: th270@cam.ac.uk


Prof. Z. Sun

QTF Centre of Excellence

Department of Applied Physics

Aalto University

FI-00076 Aalto, Finland

 The ORCID identification number(s) for the author(s) of this article can be found under <https://doi.org/10.1002/adfm.201800480>.

© 2018 The Authors. Published by WILEY-VCH Verlag GmbH & Co. KGaA, Weinheim. This is an open access article under the terms of the Creative Commons Attribution License, which permits use, distribution and reproduction in any medium, provided the original work is properly cited.

The copyright line for this article was changed on May 28, 2018, after original online publication.

DOI: 10.1002/adfm.201800480

as an economically appealing maskless deposition technique for large-area thermoelectric applications. However, stable control over the printed devices necessitates the concurrent optimization of both the thermoelectric performance of the printed material, as well as the long-term stability and suitable fluid physical properties of the material ink.

Here, we demonstrate large-area inkjet printing of graphene films for flexible thermoelectric device applications. The utilized graphene is sourced from bulk graphite exfoliated via ultrasonic-assisted liquid phase exfoliation (UALPE). Our graphene films exhibit electrical transport akin to that of few-layer graphene, however with glassy thermal transport originating from the disordered nanostructure. As a result, the thermoelectric properties of the films not only surpass those of the previous reports on all-graphene materials but are also comparable to those of the state-of-the-art graphene-conductive polymer hybrid nanocomposites produced via more intricate synthesis schemes.

## 2. Results

### 2.1. Sample Fabrication and Graphene Ink Characterization

The graphene dispersions in the present work are produced by UALPE of bulk graphite dispersed in isopropyl alcohol (IPA) with the aid of polyvinylpyrrolidone (PVP) as described in the Experimental Section. As a solvent, IPA is widely used in commercial functional and pigment-based inks, and is favored for its low boiling point (82.6 °C) promoting fast drying, and low toxicity<sup>[23]</sup> as compared to alternative solvents utilized in graphene ink formulations, such as N-methyl-2-pyrrolidone (NMP).<sup>[24]</sup> While graphene tends to quickly precipitate when dispersed into IPA alone, the added PVP stabilizes the graphene dispersion into a homogenous solution.<sup>[24]</sup> The PVP concentration is varied in the range of 0.15–1.2 mg mL<sup>-1</sup> to study its effect on the

structural and thermoelectric features of the deposited films. We measure the concentration of the graphene dispersions through absorption spectroscopy, yielding estimated graphene concentrations in the range of 0.40–0.93 mg mL<sup>-1</sup> (see the Experimental Section and Figure S1, Supporting Information). The graphene films are then fabricated with the process presented schematically in **Figure 1a**. A fixed volume of each graphene dispersion is deposited onto the target substrate followed by thermal annealing to remove the PVP stabilizer from the samples.

Atomic force microscopy (AFM) is used to characterize the morphology of the exfoliated graphene flakes. **Figure 1b** presents the thickness distribution for a representative sample of the graphene flakes, showing that 50% of the flakes have <10 nm thickness, corresponding to ≈27 layers of graphene.<sup>[25]</sup> The average lateral size of the flakes is found to be ≈200 nm (see the Experimental Section and Figure S2, Supporting Information). To confirm the quality of the exfoliated species, Raman spectroscopy of the graphene dispersions drop-cast onto SiO<sub>2</sub> substrates as performed before and after the annealing step is shown in **Figure 1c**. Both the respective spectra present singular D and G peaks with the same D/G intensity ratio of ≈0.32, indicating that graphene is not considerably affected by the annealing process.<sup>[26]</sup> Scanning electron microscope (SEM) images of typical graphene films are shown in **Figure 1d,e**, corresponding to pre- and post-annealing, respectively. We observe PVP clusters forming on the graphene films during deposition, which are then completely removed by the annealing procedure. Higher magnification SEM images, further elucidating the nanostructure of the films, are presented in **Figure S5** (Supporting Information).

### 2.2. Thermoelectric Characterization of the Graphene Films

The inks are initially optimized for thermoelectric application by spray coating 2 mL of each graphene dispersion onto

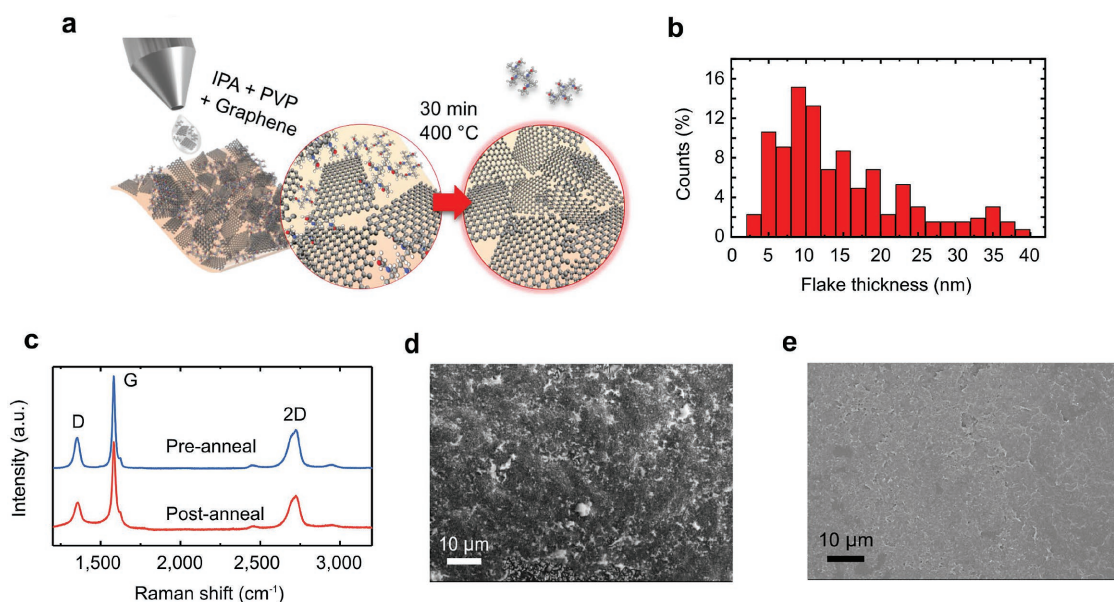


**Figure 1.** Deposition and characterization of the graphene thin films. a) Deposition and annealing scheme of the exfoliated few-layer graphene flakes suspended in an IPA/PVP solution. b) AFM thickness distribution of graphene flakes after annealing. c) Raman spectroscopy of graphene dispersions drop-cast onto SiO<sub>2</sub> pre- and post-annealing. d,e) SEM images of graphene films pre- and post-annealing, respectively.

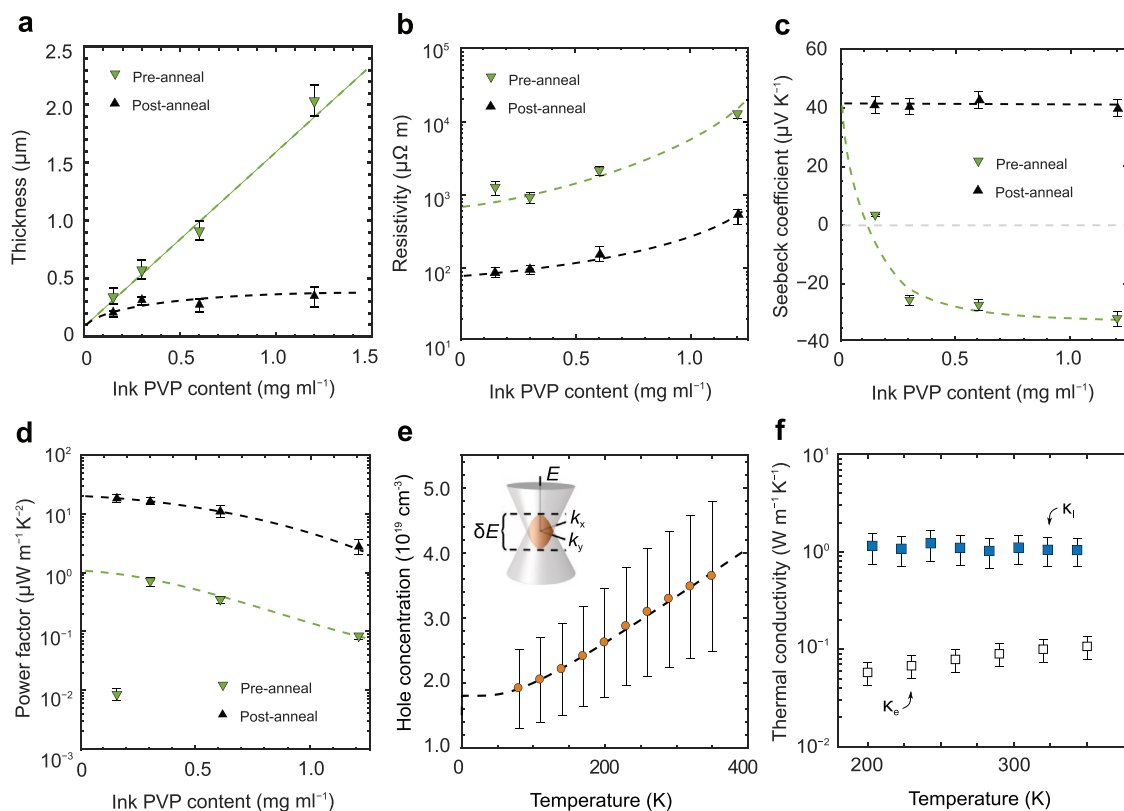


**Figure 2.** Thermoelectric and transport characterization of spray-coated graphene films. a) Thickness, b) resistivity, c) Seebeck coefficient, and d) power factor as a function of ink PVP concentration pre- and post-annealing (dashed lines indicate the overall data trends). e) Post-annealing charge concentration fitted to Equation (1) (dashed line) with band overlap energy  $\delta E = 28.1 \pm 2.3$  meV as illustrated in the inset for two parabolic bands. f) Temperature-dependent post-annealing lattice (filled symbols) and electronic (open symbols) thermal conductivities.

glass and studying the properties of the resulting films before and after PVP removal. The thermolectric properties are presented in **Figure 2**. The deposition process produces uniformly thick films with a typical standard deviation of 10–20% as determined from profilometer line scans across the films (see Figure S4, Supporting Information). As presented in Figure 2a, the thickness of the as-deposited film has an approximately linear dependence on the PVP content. The observed simultaneous preannealing increase in graphene film resistivity in Figure 2b can be similarly explained by the increase in poorly conductive PVP content in the samples. After annealing, the thickness of the film is found to be only weakly dependent on the ink PVP content, indicating that the majority of the PVP is removed, leaving a 3D network composed mostly of graphene flakes connected together via van der Waals forces. Correspondingly, the resistivity is reduced by more than an order of magnitude for all samples upon removal of the insulating PVP clusters. The improved conductivity may further be attributed to reduction of defects in the graphene film upon annealing.<sup>[27]</sup> Overall, the lowest sheet resistance values of the graphene thin films are measured at  $\approx 300 \Omega \text{ sq}^{-1}$ , which is comparable to chemical vapor deposition (CVD) grown graphene.<sup>[28]</sup>

The Seebeck coefficient measurements (shown in Figure 2c) reveal an active role of the PVP stabilizer in the intrinsic electrical properties of the graphene flakes. Initially, PVP is shown to act as a n-type chemical dopant, switching

the majority carrier type from holes to electrons in increasing the PVP content. The resulting Seebeck coefficient of the nanocomposite saturates at a value of  $\approx -32 \mu\text{V K}^{-1}$ . In fact, such chemical electron doping by PVP has been previously established in carbon nanotubes (CNT),<sup>[29]</sup> and similar spray doping of CNT thermolectric devices was recently demonstrated using polyethyleneimine (PEI) polymer.<sup>[30]</sup> After PVP removal, all samples retain a positive Seebeck coefficient of  $\approx 41 \mu\text{V K}^{-1}$ , likely due to p-type doping by atmospheric oxygen/moisture permeating the nanoporous graphene network.<sup>[31]</sup> This value is shown to be an intrinsic property of the graphene constituent, as it shows no dependency on the PVP concentration in ink.

The resulting power factor of the films,  $\text{PF} = S^2\rho^{-1}$ , is presented in Figure 2d. The power factor is found to consistently increase by over an order of magnitude upon PVP removal, and the highest power factor is achieved with the samples of smallest PVP content (0.15–0.30  $\text{mg mL}^{-1}$  in the ink). The highest value of  $18.7 \pm 4 \mu\text{W m}^{-1} \text{K}^{-2}$  is close to the extrapolated zero PVP content value ( $\approx 20 \mu\text{W m}^{-1} \text{K}^{-2}$ ) while still containing a sufficient amount of PVP to produce a stable graphene ink dispersion for aggregation prevention and long shelf-life of over several months. For the n-type material, the highest power factor of  $\approx 0.7 \mu\text{W m}^{-1} \text{K}^{-2}$  is achieved. While the performance of the n-type material could be potentially improved by, for example, optimizing the annealing process further to decrease

resistivity without losing the n-type character, we concentrate on the annealed p-type material in the remainder of this study.

### 2.3. Transport Properties of the Graphene Films

We carry out temperature-dependent Hall measurements to provide insight into the electronic structure of the films (0.30 mg mL<sup>-1</sup> PVP content). A detailed analysis of the results is presented in the Supporting Information. In brief, we measure a room-temperature charge carrier concentration of  $3.17 \times 10^{19} \text{ cm}^{-3}$  and a hole mobility of  $21.5 \text{ cm}^2 \text{ V}^{-1} \text{ s}^{-1}$  in the film. Figure 2e shows the measured carrier concentration,  $n$ , as a function of temperature at  $T = 100\text{--}350 \text{ K}$ . As the increasing carrier concentration dominates over the decrease in charge carrier mobility in the sub-room-temperature region, the resistivity of the structure shows a monotonously decreasing trend in agreement with previous work on few-layer graphene.<sup>[32]</sup> Indeed, our carrier concentration data agree well with the simple two-band (STB, see inset of Figure 2e) model commonly utilized for few-layer graphene<sup>[32]</sup>

$$n = C_0 k_B T \ln \left( 1 + \exp \left( \frac{\delta E}{2k_B T} \right) \right) \quad (1)$$

where  $C_0$  is a constant,  $k_B$  denotes the Boltzmann constant, and  $T$  is the temperature. The carrier concentrations are in excellent agreement with the model at a valence and conduction band overlap energy,  $\delta E$ , of  $\approx 28.1 \pm 2.3 \text{ meV}$  (dashed line in Figure 2e). This suggests that the temperature-dependent electrical transport behavior is dictated by the few-layer graphene flakes and, therefore, not altered by the disordered structure of the film. In reference to Figure 1b, the Hall measurement thus confirms that the electrical transport mechanism of the samples matched the assumed few-layer composition as characterized in the graphene inks by AFM.

To further assess thermal transport mechanisms within the structure, we measure temperature-dependent thermal conductivity using an optical pump-probe method. We note that the nanosecond transient thermoreflectance (TTR, see the Experimental Section and the Supporting Information) method utilized for measuring thermal diffusivity is strictly limited for analyzing the cross-plane thermal conductivity of planar samples. While the thermal properties on graphene are known to be highly anisotropic,<sup>[13]</sup> we expect that the measurement provides a reasonable estimate to the extent that the stochastic deposition process promotes mixing of in-plane and cross-plane contributions of individual flakes.

The temperature-dependent lattice and electronic contributions to the thermal conductivity are presented in Figure 2f. The electronic thermal conductivity contributed by charge carriers is estimated by the use of the Wiedemann-Franz law,<sup>[33]</sup>  $\kappa_e = L T \rho^{-1}$ , where  $L = 2.44 \times 10^{-8} \text{ W } \Omega \text{ K}^{-2}$  is the Lorenz number. The electronic contribution is then subtracted from the measured total thermal conductivity to extract the lattice thermal conductivity,  $\kappa_l$ . We measure a rather low room-temperature thermal conductivity of  $1.00 \pm 0.25 \text{ W m}^{-1} \text{ K}^{-1}$  for the structure, of which less than 8% is contributed by charge carriers. Evidently, the effective thermal conductivity is reduced far

below that of intraflake transport, approaching typical values reported for graphene-polymer nanocomposites.<sup>[34]</sup> The modest temperature dependence further suggests that thermal transport is dominated by interface scattering within the disordered structure rather than by intraflake phonon transport. Such observation is in agreement with recent numerical and experimental studies on 3D graphene laminates, showing strongly suppressed thermal conductivity in decreasing the lateral size of the graphene flakes.<sup>[35,36]</sup> Thus, the low effective thermal conductivity is expected to result from the nanoporous structure in combination with the relatively small average lateral flake size. The resulting estimated room-temperature  $zT$  is of the order of  $10^{-3}$ . Owing to the disordered structure, the films thus exhibit effective characteristics conforming to the phonon-glass electron-crystal paradigm,<sup>[37]</sup> in which electronic conduction governed by a well-defined band structure coincides with glass-like phonon transport.

### 2.4. Inkjet Printed Large-Area Thermoelectric Devices

Drop-on-demand inkjet printing provides a promising solution for controllable and cost-effective deposition of nanomaterials. Stable drop generation and jetting of ink are crucial requirements for high-quality inkjet printing. Therefore, the printing conditions are specifically optimized for the formulated thermoelectric graphene ink. The printability of the ink is usually predicted by the inverse Ohnesorge number  $Z = (\gamma d \alpha)^{1/2} \eta^{-1}$ , where  $\gamma$  is the surface tension ( $\text{mN m}^{-1}$ ),  $d$  is the density ( $\text{g cm}^{-3}$ ),  $\eta$  is the viscosity ( $\text{mPa s}$ ) of the ink, and  $\alpha$  denotes the inkjet nozzle diameter ( $\mu\text{m}$ ). As a guide, the  $Z$  value should be between 1 and 14 to avoid formation of long filament or secondary/satellite droplets.<sup>[38]</sup> Pendant drop measurements and parallel plate rheometry are performed to ascertain  $\gamma$  and  $\eta$  for the graphene ink at room temperature, measured at  $\approx 28 \text{ mN m}^{-1}$  and  $\approx 2.3 \text{ mPa s}$ , respectively. With a density of  $\approx 0.8 \text{ g cm}^{-3}$  and nozzle diameter of  $22 \mu\text{m}$ , we therefore calculate  $Z = 9.6$  for our ink, suggesting that the ink allows high stability in printing. Observation of jetting sequences for our ink confirms this, demonstrating a stable process without the formation of satellite droplets or long filaments during printing (see Figure S3a, Supporting Information). We also investigate the optimal printing conditions of our ink with respect to temperatures of the substrates and the spacing of printed droplets. We find that uniform printing is achieved through a droplet spacing of  $35 \mu\text{m}$  at a substrate temperature of  $60 \text{ }^\circ\text{C}$  (see Figure S3b,c, Supporting Information). The thermoelectric power factor of the printed films is measured at  $18.7 \pm 3.3 \mu\text{W m}^{-1} \text{ K}^{-2}$  and thus independent of the deposition method used.

Examples of intricate graphene patterns inkjet printed onto a clear and flexible polyethylene terephthalate (PET) substrate under the optimized printing conditions are presented in Figure 3a. As a demonstration of a functional all-printed thermoelectric device, we prepare a device consisting of 20 inkjet-printed graphene legs connected by inkjet-printed silver (Ag, see inset of Figure 3c) as shown in Figure 3b. The large-area device is printed on flexible Kapton polyimide and is thus suited for conforming onto nonplanar surfaces or for harvesting energy from body heat in wearable applications. To confirm

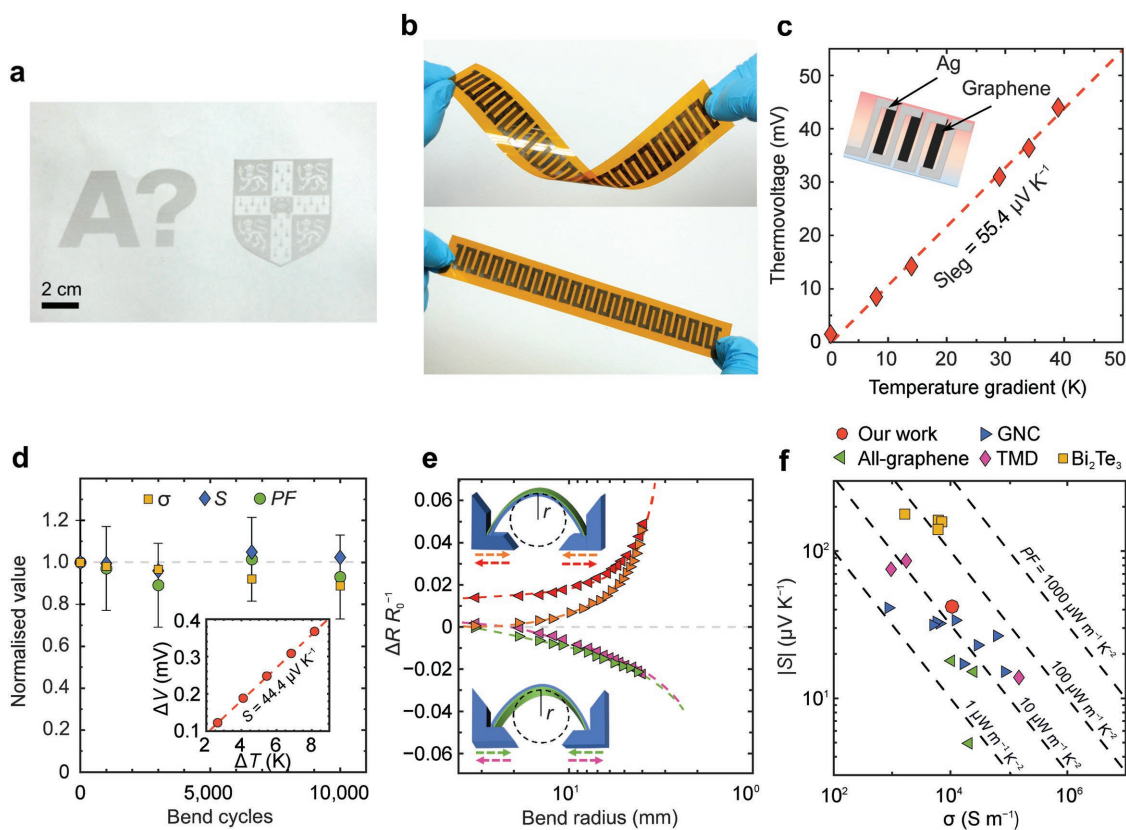


**Figure 3.** Inkjet-printed thermoelectric device and performance review. a) A photograph of inkjet-printed graphene patterns on a flexible PET substrate. b) Photographs of an inkjet-printed device consisting of 20 silver and graphene legs bent (above) and as is (below). c) Voltage response of the device as a function of temperature gradient. Inset: a schematic image of the printed device geometry. d) Relative change in a single graphene leg thermoelectric performance as a function of bend cycles (error bars shown for power factor). Inset: Seebeck coefficient measurement of the undeformed film. e) Relative change in a single graphene leg resistance as a function of bend radius under tensile (upper inset) and compressive (lower inset) bending as indicated by the colored arrows. f)  $|S|$  versus  $\sigma$  of the present work and values reported for large-area solution-processed graphene, other 2D material, and graphene-conductive polymer films. Dashed lines represent contours of constant power factor.

the performance of the device, it is bent in a ring shape and positioned onto a heated hot plate with one side in contact with the heated surface. The thermovoltage responses arising from the imposed thermal gradients over the device as measured by separate thermocouples are presented in Figure 3c. The device exhibits a linear voltage response as a function of temperature difference between the opposing edges of the device, demonstrating the potential of the inkjet-printed graphene-based thermoelectric devices for flexible and wearable applications. The corresponding Seebeck coefficient of a single leg is calculated at  $55.4 \mu\text{V K}^{-1}$ , which is moderately higher but similar to that characterized in a controlled atmosphere (see the Experimental Section). Further, as the hot side of the device reaches temperatures as high as 385 K during the characterization, the device shows excellent thermostability in ambient air.

To quantify the feasibility of utilizing such printed devices for flexible thermoelectronic applications, the stability of the thermoelectric performance of a single leg is monitored under periodic and repetitive mechanical stress: an annealed film printed onto Kapton polyimide is bent to a radius of  $\approx 4.5$  mm and released for up to 10 000 times, during which the Seebeck coefficient, conductivity ( $\sigma = \rho^{-1}$ ), and power factor are compared with those of the undeformed film as

shown in Figure 3d. In considering the error estimates in the measurement, no change can be resolved to take place during the continuous deformation of 10 000 bending cycles, indicating high flexibility and stability against mechanical deformation.

Similarly, the resistance of the films is measured under mechanical stress in collapsed radius tests (see the Experimental Section), and a representative result is presented in Figure 3e. The resistance of the film is typically changed by  $<10\%$  at a considerable bend radius ( $<4$  mm), suggesting that the graphene films are very well suited for flexible thermoelectronics applications. For reference, a recent report on free-standing all-graphene films showed a complete fracture of the film at a bending radius of 8 mm,<sup>[22]</sup> while a modest bending radius of 20 mm has been achieved for thermoelectric devices utilizing traditional solid-state materials.<sup>[6]</sup> The change in the resistance of the graphene films is further found to be reversible, and positive or negative in sign depending on whether tensile or compressive bending is imposed, respectively. These findings point to the conclusion that the change in resistance is not due to breaking of the films, but rather associated with density change in the nanoporous film under mechanical deformation.

### 3. Discussion

To set the findings into a more general context, we provide a visual comparison between our results and several recent studies on room-temperature thermoelectric properties of solution-processed graphene structures,<sup>[22,39]</sup> transition metal dichalcogenides (TMD),<sup>[40,41]</sup> graphene-conductive polymer organic hybrid nanocomposites (GNC),<sup>[34,39,42–45]</sup> and printed Bi<sub>2</sub>Te<sub>3</sub>.<sup>[46,47]</sup> While we recognize that CNT-based solutions have shown persistently outstanding performance as compared to graphene due to well-established selective synthesis routes and tunable bandgap, graphene is merited by its considerably lower cost and suitability for stable, large-area device processing.<sup>[48]</sup>

Figure 3f shows a scatter plot of the reported Seebeck coefficient values as a function of electrical conductivity. The diagonal dashed lines represent contours of constant thermoelectric power factor (increasing toward the upper right corner of the figure). In the scarcity of studies on all-graphene structures, our results mark the best thermoelectric power factor at an  $\approx 230\%$  improvement, further achieving the highest Seebeck coefficient among the solution-processed graphene structures. While the performance is found to be similar to those of state-of-the-art GNCs, the thermostability and mechanical durability of all-graphene structures present a clear advantage over polymeric materials. Indeed, the all-graphene films are produced via annealing at 670 K, and the resistivity of the films shows modest temperature dependence in the range of  $T = 100\text{--}600$  K at a variation within  $<15\%$  from the room-temperature value (Figure S6a, Supporting Information). In contrast, the most widely utilized conductive polymer poly(3,4-ethylenedioxythiophene) (PEDOT) sustains its thermoelectric features at a maximum temperature of 370 K.<sup>[4]</sup> Within the presented 2D TMDs, our results surpass the inorganic semiconducting MoS<sub>2</sub> and WS<sub>2</sub> with high  $S$  ( $\approx 80 \mu\text{V K}^{-1}$ ) but low  $\sigma$ , while the metallic NbSe<sub>2</sub> is shown to be moderately higher in performance due to its high  $\sigma$  regardless of its low  $S$  ( $\approx 14 \mu\text{V K}^{-1}$ ). While highest in performance, solution-processed Bi<sub>2</sub>Te<sub>3</sub> suffers from the same shortcomings as its bulk counterpart. Due to the comparable thermal conductivities as reported for graphene-polymer nanocomposites,<sup>[34]</sup> all-graphene structures are expected to provide further improvement in thermoelectric performance through increasing the power factor by, for example, optimized layering<sup>[28,49]</sup> and nanostructuring.<sup>[12]</sup> Moreover, designing stable chemical doping schemes can be considered simultaneously important for future progress.

### 4. Conclusion

In summary, we have presented large-area inkjet printing as a maskless, cost-effective, and facile fabrication route for nanoporous graphene thin films for thermoelectric applications. Both n- and p-type charge transport are achieved within the same process by controlling the polymer additive PVP content of the graphene films. We demonstrate that the all-graphene structure has thermoelectric performance similar to state-of-the-art graphene-conductive polymer nanocomposites, arising from the electronic structure of few-layer graphene combined with a low thermal conductivity, constituting the phonon-glass

electron-crystal character of the films. The inks are further suitable for inkjet-printed thermoelectric devices, showing exceptional thermostability and durability against mechanical deformation for over 10 000 bending cycles. Thus, our work constitutes a highly potential approach for ecologically and economically viable all-printed thermoelectric devices.

### 5. Experimental Section

*Graphene Ink Production, Characterization, and Inkjet Printing:* Graphene dispersions are formulated via the UALPE technique by mixing graphite crystals (200 g, 100 mesh flakes, Sigma-Aldrich) and PVP (3, 6, 12, and 24 mg, average molecular weight 10 000 Da, Sigma-Aldrich) with IPA (20 mL). The mixture was sonicated in a bath sonicator for 12 h. During the exfoliation process, the bath temperature was kept at  $\approx 15^\circ\text{C}$ . After this, the dispersion was centrifuged for 1 h at 4030 rpm ( $1540 \times g$ ) to separate the few-layer graphene species from the unexfoliated content. The top 70% of the supernatant graphene dispersion was then collected and used in the experiments. The concentration of the dispersed graphene was estimated from optical absorption spectroscopy at 660 nm using the Beer–Lambert law. Before the characterization, the graphene dispersion was diluted down to 10 vol% to avoid scattering losses during absorption characterization.<sup>[50]</sup> Samples for Raman measurement were prepared by drop-casting graphene dispersions onto a Si/SiO<sub>2</sub> substrate (SiO<sub>2</sub> thickness  $\approx 285$  nm). Raman characterization of the graphene/PVP composites (pre- and post-annealing) was performed at an excitation wavelength of 514 nm with  $<0.1$  mW power for each measurement point so as not to damage the graphene flakes. The intensities were normalized to that of the G-peak. The thickness distribution of the dispersed graphene was characterized by AFM. Before measurement, the graphene dispersions were diluted to 2 vol% by pure IPA. The Si/SiO<sub>2</sub> substrate was then dip-coated into diluted dispersion, followed by a thermal annealing step at 400 °C for 30 min, used for all annealed samples in the present study. The sample was imaged with a Bruker Dimension Icon AFM in ScanAsyst mode using a silicon cantilever with a Si<sub>3</sub>N<sub>4</sub> tip. The surface tension and the viscosity of the ink ( $0.15 \text{ mg mL}^{-1}$  PVP content) were characterized through pendant droplet and parallel plate rheometer measurements (TA Instrument Discovery HR-1) at 15 °C with shear range  $1\text{--}1000 \text{ s}^{-1}$ . The density of the ink was measured by weighing it in known volumes. The inkjet printer used in this work is a Fujifilm Dimatix DMP-2831, and the cartridge is Dimatix DMC-11610 which produces  $\approx 10$  pL droplets.

*Mechanical Characterization of the Graphene Films:* The thickness of the films was measured using Dektak 3 Surface Profilometer from five positions along the film to achieve a statistical estimate for the average thickness. As uncertainty in the film thickness is found to be the most prominent source of uncertainty in the measurements,<sup>[51]</sup> the standard deviation of individual thickness measurements was used to quantify the resulting experimental error. Flexibility of the graphene films were analyzed through collapsed radius tests,<sup>[52]</sup> for which the samples were deposited onto a flexible Kapton polyimide substrate, freely suspended between two motorized micro stages. Assuming a sinusoidal shape, the bend radius of the film may be approximated from the separation between the stages. The corresponding relative change in resistance was obtained from an  $I$ – $V$  curve measured by Keithley 2401 30 s after moving the stage in order to avoid transient effects related to the applied mechanical stress.

*Thermoelectric and Transport Measurements:* Linseis LSR3 Seebeck coefficient measurement system equipped with a thin film adapter was used for measuring the Seebeck coefficient and resistivity of the thin films at an average temperature of 34 °C in helium atmosphere. Resistivity was measured using a four-point contact geometry. In the Seebeck coefficient measurement, five different temperature gradients were imposed over the sample and the resulting thermovoltage was recorded. The measurement was repeated five times and a linear curve was fitted onto the resulting data in order to extract the Seebeck

coefficient from the slope of the curve (see inset of Figure 3d). For temperature-dependent mobility and charge carrier concentration measurements, Ecopia HMS-5300 Hall measurement system was used with the van der Pauw contact geometry. 30 nm/40 nm titanium/gold contacts were utilized throughout the electrical measurements, with  $4 \times 20$  and  $11 \times 11$  mm glass substrates for Seebeck and Hall measurements, respectively.

**Thermal Conductivity Measurement:** Linseis Thinfilmlaser Laserflash Analyser (TF-LFA) was used for determining the thermal conductivity of the graphene films after the annealing process. For preparing a sample for the measurement, it was deposited onto (110) silicon chips and coated with 20 nm Ti followed by 200 nm of Au for adhesion and transducer layers, respectively. A thinner  $\approx 65$  nm sample was used in favor of smoother surface. The equipment utilizes the nanosecond transient TTR method,<sup>[53]</sup> in which an  $\approx 8$  ns pulse as generated by an Nd:YAG pump laser (1064 nm, 10 Hz) was used for heating the gold transducer layer on top of the sample structure. The reflectance of the gold layer was monitored using a diode pumped solid-state probe laser (25 mW) at a wavelength of 463 nm. At this wavelength, the reflectance of gold is proportional to its temperature, and the transient decay of the heat induced reflectivity change is associated with the thermophysical properties of the underlying structure. A single measurement consists of triggering 50 pulses and averaging over the resulting signals. Heat flow within the structure was then modeled using 1D transmission-line formalism, and fitted to the experimental data by using genetic algorithm in order to extract the thermal conductivity of the graphene film (see the Supporting Information for details).<sup>[54]</sup> The measurements were carried out on six positions over the sample area in order to further average over the spatial variation caused by the solution-based deposition process. All metallic coatings were deposited by electron beam evaporation (Varian).

## Supporting Information

Supporting Information is available from the Wiley Online Library or from the author.

## Acknowledgements

This research was partly performed at the Micronova Nanofabrication Centre, supported by Aalto University. T.J. acknowledges the financial support from the Aalto ELEC Doctoral School, H.J. from Jenny ja Antti Wihuri Foundation, T.A.O. from EPSRC grant EP/L016087/1, T.H. from RAEng through a research fellowship (Graphlex), Z.S. from Academy of Finland (Grant Nos. 276376, 284548, 295777, 304666, 312551, 312297, and 314810), the European Union's Seventh Framework Programme (Grant No. 631610), the Tekes Projects (OPEC), and the Nokia Foundation, and I.T. from Academy of Finland (Grant No. 285972) and European Union's Horizon 2020 Programme (Grant No. 645241).

## Conflict of Interest

The authors declare no conflict of interest.

## Keywords

graphene, inkjet printing, large-area thermoelectrics

Received: January 19, 2018  
Revised: March 15, 2018  
Published online: April 19, 2018

- [1] M. S. Dresselhaus, G. Chen, M. Y. Tang, R. Yang, H. Lee, D. Wang, Z. Ren, J.-P. Fleurial, P. Gogna, *Adv. Mater.* **2007**, *19*, 1043.
- [2] L. Hicks, M. Dresselhaus, *Phys. Rev. B* **1993**, *47*, 12727.
- [3] Q. Zhang, Y. Sun, W. Xu, D. Zhu, *Adv. Mater.* **2014**, *26*, 6829.
- [4] Y. Chen, Y. Zhao, Z. Liang, *Energy Environ. Sci.* **2015**, *8*, 401.
- [5] K. Biswas, J. He, G. Wang, S.-H. Lo, C. Uher, V. P. Dravid, M. G. Kanatzidis, *Energy Environ. Sci.* **2011**, *4*, 4675.
- [6] S. J. Kim, J. H. We, B. J. Cho, *Energy Environ. Sci.* **2014**, *7*, 1959.
- [7] R. Venkatasubramanian, E. Siivola, T. Colpitts, B. O'quinn, *Nature* **2001**, *413*, 597.
- [8] F. Bonaccorso, Z. Sun, T. Hasan, A. Ferrari, *Nat. Photonics* **2010**, *4*, 611.
- [9] K. I. Bolotin, K. Sikes, Z. Jiang, M. Klima, G. Fudenberg, J. Hone, P. Kim, H. Stormer, *Solid State Commun.* **2008**, *146*, 351.
- [10] C. Lee, X. Wei, J. W. Kysar, J. Hone, *Science* **2008**, *321*, 385.
- [11] Z. Sun, T. Hasan, F. Torrisi, D. Popa, G. Privitera, F. Wang, F. Bonaccorso, D. M. Basko, A. C. Ferrari, *ACS Nano* **2010**, *4*, 803.
- [12] P. Dollfus, V. H. Nguyen, J. Saint-Martin, *J. Phys. Condens. Matter* **2015**, *27*, 133204.
- [13] E. Pop, V. Varshney, A. K. Roy, *MRS Bull.* **2012**, *37*, 1273.
- [14] Y. Ouyang, J. Guo, *Appl. Phys. Lett.* **2009**, *94*, 263107.
- [15] Y. Yokomizo, J. Nakamura, *Appl. Phys. Lett.* **2013**, *103*, 113901.
- [16] P.-H. Chang, B. K. Nikolić, *Phys. Rev. B* **2012**, *86*, 041406.
- [17] H. Karamitaheri, N. Neophytou, M. Pourfath, R. Faez, H. Kosina, *J. Appl. Phys.* **2012**, *111*, 054501.
- [18] J. Haskins, A. Kınacı, C. Sevik, H. Sevinçli, G. Cuniberti, T. Çağın, *ACS Nano* **2011**, *5*, 3779.
- [19] H. Sevinçli, C. Sevik, T. Çağın, G. Cuniberti, *Sci. Rep.* **2013**, *3*, 1228.
- [20] A. Dey, O. P. Bajpai, A. K. Sikder, S. Chattopadhyay, M. A. S. Khan, *Renewable Sustainable Energy Rev.* **2016**, *53*, 653.
- [21] G. Chen, W. Xu, D. Zhu, *J. Mater. Chem. C* **2017**, *5*, 4350.
- [22] Y. Guo, J. Mu, C. Hou, H. Wang, Q. Zhang, Y. Li, *Carbon* **2016**, *107*, 146.
- [23] G. Hu, T. Albrow-Owen, X. Jin, A. Ali, Y. Hu, R. C. T. Howe, K. Shehzad, Z. Yang, X. Zhu, R. I. Woodward, T.-C. Wu, H. Jussila, J.-B. Wu, P. Peng, P.-H. Tan, Z. Sun, E. J. R. Kelleher, M. Zhang, Y. Xu, T. Hasan, *Nat. Commun.* **2017**, *8*, 278.
- [24] S. Santra, G. Hu, R. Howe, A. De Luca, S. Ali, F. Udrea, J. Gardner, S. Ray, P. Guha, T. Hasan, *Sci. Rep.* **2015**, *5*, 17374.
- [25] A. Gupta, G. Chen, P. Joshi, S. Tadigadapa, P. C. Eklund, *Nano Lett.* **2006**, *6*, 2667.
- [26] A. C. Ferrari, J. C. Meyer, V. Scardaci, C. Casiraghi, M. Lazzeri, F. Mauri, S. Piscanec, D. Jiang, K. S. Novoselov, S. Roth, A. K. Geim, *Phys. Rev. Lett.* **2006**, *97*, 1.
- [27] E. B. Secor, T. Z. Gao, A. E. Islam, R. Rao, S. G. Wallace, J. Zhu, K. W. Putz, B. Maruyama, M. C. Hersam, *Chem. Mater.* **2017**, *29*, 2332.
- [28] X. Li, J. Yin, J. Zhou, Q. Wang, W. Guo, *Appl. Phys. Lett.* **2012**, *100*, 183108.
- [29] Y. Nonoguchi, K. Ohashi, R. Kanazawa, K. Ashiba, K. Hata, T. Nakagawa, C. Adachi, T. Tanase, T. Kawai, *Sci. Rep.* **2013**, *3*, 3344.
- [30] D. S. Montgomery, C. A. Hewitt, R. Barbalace, T. Jones, D. L. Carroll, *Carbon* **2016**, *96*, 778.
- [31] S. Ryu, L. Liu, S. Berciaud, Y.-J. Yu, H. Liu, P. Kim, G. W. Flynn, L. E. Brus, *Nano Lett.* **2010**, *10*, 4944.
- [32] K. Nagashio, T. Nishimura, K. Kita, A. Toriumi, *Jpn. J. Appl. Phys.* **2010**, *49*, 051304.
- [33] G. S. Nolas, J. Sharp, H. J. Goldsmid, *Thermoelectrics: Basic Principles and New Materials Developments*, Springer-Verlag, Berlin, Germany **2001**.
- [34] B. Abad, I. Alda, P. Díaz-Chao, H. Kawakami, A. Almarza, D. Amantia, D. Gutierrez, L. Aubouy, M. Martín-González, *J. Mater. Chem. A* **2013**, *1*, 10450.
- [35] H. Malekpour, K.-H. Chang, J.-C. Chen, C.-Y. Lu, D. Nika, K. Novoselov, A. Balandin, *Nano Lett.* **2014**, *14*, 5155.
- [36] B. Mortazavi, T. Rabczuk, *Carbon* **2015**, *85*, 1.

- [37] G. Slack, in *CRC Handbook of Thermoelectrics* (Ed: D. M. Rowe), CRC Press, Boca Raton, FL **1995**.
- [38] D. Jang, D. Kim, J. Moon, *Langmuir* **2009**, *25*, 2629.
- [39] J. Xiang, L. T. Drzal, *Polymer* **2012**, *53*, 4202.
- [40] T. Wang, C. Liu, J. Xu, Z. Zhu, E. Liu, Y. Hu, C. Li, F. Jiang, *Nanotechnology* **2016**, *27*, 285703.
- [41] J. Y. Oh, J. H. Lee, S. W. Han, S. S. Chae, E. J. Bae, Y. H. Kang, W. J. Choi, S. Y. Cho, J.-O. Lee, H. K. Baik, T. I. Lee, *Energy Environ. Sci.* **2016**, *9*, 1696.
- [42] Y. Du, S. Z. Shen, W. Yang, R. Donelson, K. Cai, P. S. Casey, *Synth. Met.* **2012**, *161*, 2688.
- [43] K. Xu, G. Chen, D. Qiu, *J. Mater. Chem. A* **2013**, *1*, 12395.
- [44] D. Yoo, J. Kim, J. H. Kim, *Nano Res.* **2014**, *7*, 717.
- [45] L. Wang, Q. Yao, H. Bi, F. Huang, Q. Wang, L. Chen, *J. Mater. Chem. A* **2014**, *2*, 11107.
- [46] Z. Lu, M. Layani, X. Zhao, L. P. Tan, T. Sun, S. Fan, Q. Yan, S. Magdassi, H. H. Hng, *Small* **2014**, *10*, 3551.
- [47] A. Chen, D. Madan, P. Wright, J. Evans, *J. Micromech. Microeng.* **2011**, *21*, 104006.
- [48] N. Liu, F. Luo, H. Wu, Y. Liu, C. Zhang, J. Chen, *Adv. Funct. Mater.* **2008**, *18*, 1518.
- [49] V. H. Nguyen, M. C. Nguyen, H.-V. Nguyen, J. Saint-Martin, P. Dollfus, *Appl. Phys. Lett.* **2014**, *105*, 133105.
- [50] C. F. Bohren, D. R. Huffman, *Absorption and Scattering of Light by Small Particles*, Wiley-VCH, Weinheim, Germany **1998**.
- [51] H. Jussila, T. Albrow-Owen, H. Yang, G. Hu, S. Aksimsek, N. Granqvist, H. Lipsanen, R. C. T. Howe, Z. Sun, T. Hasan, *ACS Omega* **2017**, *2*, 2630.
- [52] S.-I. Park, J.-H. Ahn, X. Feng, S. Wang, Y. Huang, J. A. Rogers, *Adv. Funct. Mater.* **2008**, *18*, 2673.
- [53] S. Ali, T. Juntunen, S. Sintonen, O. M. Ylivaara, R. L. Puurunen, H. Lipsanen, I. Tittonen, S.-P. Hannula, *Nanotechnology* **2016**, *27*, 445704.
- [54] G. Chen, P. Hui, *Thin Solid Films* **1999**, *339*, 58.